

Dynamic fracture of glass fiber-reinforced ductile polymer matrix composites and loading rate effect

Jinling Gao^a, Nesredin Kedir^b, Julio A. Hernandez^a, Jian Gao^c, Todd Horn^d, Garam Kim^d, Kamel Fezzaa^e, Tyler N. Tallman^a, Giuseppe Palmese^c, Ronald Sterkenburg^d, Weinong Chen^{a,b,*}

Abstract: The dynamic fracture of S-2 glass fiber-reinforced polymer matrix composites (FRPMCs) was investigated in this study. The matrix ductility was improved by a recently developed network topology modification technique via mixing partially reacted substructures (mPRS). The composite material was manufactured and characterized by micro-CT scanning and scanning electron microscopy (SEM). Dynamic single-edge notched bending (d-SENB) experiments were performed on the composites by using a modified split-Hopkinson pressure bar. Each specimen's fracture process was visualized by ultrafast X-ray imaging. Such *in-situ* radiography enabled identifying the damage initiation below 50-micron scale and inspecting its propagation through the internal structures of opaque composites, thereby accurately quantifying the composites' mechanical properties. Furthermore, the identical d-SENB experiments were designed and the digital image correlation (DIC) was employed to monitor the stress wave propagation on the composite specimens. The force and deflection measurements were modified and correlated to the physical damage processes. Besides, quasi-static SENB experiments were conducted to identify the loading rate effects on the composites' fracture behaviors. The force and deflection history, bending stiffness, energy dissipation, and fracture toughness at different loading rates were quantified and compared. Finally, post-fracture analysis by micro-CT scanning and SEM provided physical observations on the variation of the fracture morphology by different loading rates.

Keywords: Ductile matrix; FRPMCs; Fracture behavior; Loading rate effect; Ultrafast X-ray imaging.

* Corresponding author, email: wchen@purdue.edu

^a School of Aeronautics and Astronautics, Purdue University, 701 W Stadium Avenue, West Lafayette, IN, 47907, USA

^b School of Materials Engineering, Purdue University, 701 W Stadium Avenue, West Lafayette, IN, 47907, USA

^c Department of Chemical and Biological Engineering, Drexel University, 3101 Ludlow Street, Philadelphia, PA, 19104, USA

^d Indiana Manufacturing Institute, Purdue University, 1105 Challenger Avenue, West Lafayette, IN, 47906, USA

^e Advanced Photon Source, Argonne National Laboratory, 9700 South Cass Avenue, Argonne, IL 60439, USA

1 **1. Introduction**

2 Fiber-reinforced polymer matrix composites (FRPMCs) are substantially utilized in military
3 vehicle armors to replace metals because of their competitive advantage of light weight. They are
4 also strong, stiff, and corrosion- and fatigue-resistant [1-2]. However, compared with metals,
5 FRPMCs are essentially brittle, thereby being susceptible to the damage under impact [3].
6 Furthermore, the anisotropy and heterogeneity of composite materials and uneven stress
7 distribution under the transient loading can complicate the damage process [4]. Therefore, except
8 for energy dissipation, the impact-induced damage has been a critical safety concern for FRPMCs
9 in dynamic environments.

10 This study aims to investigate the dynamic damage evolution in an S-2 glass fiber-reinforced
11 ductile polymer matrix composite under dynamic loadings, characterize the impact-induced
12 damage, and quantify its energy dissipation and fracture properties. The matrix was made by
13 modifying the TGDDM-Jeffamine[®] D230 via a monoamine partially reacted substructures
14 (mPRS), which reduces the crosslink density locally to mimic the collapsed voids and produces a
15 toughened epoxy system. Simultaneously, mPRS could also create a local concentration of chain
16 ends that were covalently bound to the free polymer network, thereby increasing the epoxy
17 system's ductility [5-6]. The matrix's stress-strain curves and mechanical properties were
18 measured at different strain rates and reported in the previous research, as shown in Fig. 1 and
19 Table 1, respectively. It is revealed that the matrix had an increasingly non-linear behavior as the
20 strain increased before a stress peak was reached. At lower strain rates, after the peak stress, the
21 matrix experienced strain softening and subsequent strain hardening. In contrast, only strain
22 softening was observed when the loading rate was high. Such a rate-dependent stress-strain
23 behavior is presumably because the adiabatic heating at the high strain rate suppressed the strain
24 hardening when the polymer chains were aligned at the low strain rate [7-8]. On the other hand,
25 the reinforcement S-2 glass fibers are also reported to have strain-rate-dependent behaviors in both
26 longitudinal and transverse directions [9]. Therefore, considering the strain rate effect on the
27 reinforcement and matrix's mechanical response, it is necessary to investigate the composite
28 material at different loading rates.

29 The composite specimens were first prepared and then characterized by using micro-CT scanning
30 and scanning electron microscope (SEM) to identify the fiber distribution and defects and measure
31 the fiber volume fraction prior to the mechanical experiments. An advanced imaging technique,

1 ultrafast X-ray imaging, was used to visualize the time-resolved damage evolution within the
2 opaque S-2 glass/TGDDM-Jeffamine[®] D230 + mPRS composites. Being integrated into the
3 dynamic single-edge notched bending (d-SENB) experiments which were designed on a modified
4 split-Hopkinson pressure bar, such a technique enables capturing the damage initiation and
5 propagation inside the composites with a high spatial and temporal resolution [10-11]. Furthermore,
6 additional dynamic loading experiments were conducted, and the digital imaging correlation (DIC)
7 was used to track the stress wave propagation in the composites. The force and deflection
8 measurements were then corrected and correlated with the physical damage process, providing
9 more accurate assessment on the composites' fracture properties. Additional loading experiments
10 include SENB experiments at two different quasi-static loading rates. The composites' force and
11 deflection responses, energy dissipation, stiffness, and fracture toughness at different loading rates
12 were quantified and compared. Finally, post-fracture analysis by micro-CT scanning and scanning
13 electron microscope (SEM) provided the physical characterizations on the rate-related composites'
14 fracture behaviors.

15

16 **2. Materials**

17 The fiber reinforcements, S-2 glass 463AA-1250, was provided by AGY (Aiken, SC, USA) in
18 roving. The matrix system included the epoxy TGDDM purchased from Sigma-Aldrich (St. Louis,
19 MO, USA) and the primary curing agent, Jeffamine[®] D230, supplied by Huntsman Corporation
20 (The Woodlands, TX, USA). The mPRS was synthesized by partially curing TGDDM and
21 Jeffamine[®] M1000 at a 75% conversion [5-6].

22 In many composites with different stacking manners, unidirectional composites have the simplest
23 layup structure and can include many fundamental failure mechanisms when subjected to external
24 loadings [12-13]. Experimental investigations on unidirectional composites usually provide the
25 basic mechanical properties and reliable results convenient for model validation [14-15]. Therefore,
26 in this study, SENB experiments were conducted on unidirectional composites.

27 To prepare the specimens, a unidirectional composite laminate needed to be manufactured. The
28 first step is to fabricate the unidirectional fabrics as reinforcements and prepare the matrix for
29 dispersion. The unidirectional S-2 glass fabrics were obtained by winding the roving on a lab-
30 constructed filament winding setup [10]. The fabrics were not stitched to avoid any potential effect
31 on the composites' mechanical properties [16-17]. Considering the epoxy/amine equivalent weight

1 of TGDDM and Jeffamine[®] D230 to be 105.63 and 59.52, respectively, the epoxy TGDDM and
2 curing agent Jeffamine[®] D230 was mixed at a weight ratio of 1:1. The mPRS was then added into
3 the mixture at a percent by weight of 15%. The TGDDM, Jeffamine[®] D230, and mPRS were then
4 well stirred, followed by a 30-minute vacuum-assisted bubble removal process at a pressure of
5 ~0.1 kPa and room temperature. The second step was to wet the unidirectional fabrics with the
6 prepared matrix and obtain the S-2 glass fiber prepregs. Next, the prepregs were stacked, vacuum
7 bagged, and cured at 80 °C and 80 kPa in an environmental chamber for 24 hours. The post-curing
8 procedure took 4 hours by treating the laminate at a temperature of 160 °C and atmosphere pressure
9 [18].

10 The small composite specimens were obtained by cutting the unidirectional composite laminate
11 using either a diamond blade (UKAM Industrial Superhard Tools, Valencia, CA, USA) or a surface
12 grinder. The design of the specimen's dimensions was schematically described in Fig. 2, which is
13 based on the international standard ASTM D5045-14 [19]. The notch was created at the specimen's
14 middle length (L) with a depth of 45% - 50% H by using the diamond blade. Two specimen types
15 were cut from the composite laminate: 0° composites with fibers oriented in L direction and 90°
16 composites with fibers along B direction. The dimensions and notch depths in average are listed
17 in detail in Table 2.

18

19 **3. Experiments**

20 3.1. Material characterization prior to mechanical experiments

21 To characterize the microstructures of the composite and determine the fiber volume fraction, a
22 Skyscan1272 X-ray micro-CT scanner (Bruker, MA, USA) was used to perform three-dimensional
23 (3D) computed tomography on the unnotched specimens. In each scan, a specimen was mounted
24 on an ultra-precision air-bearing stage free of motion and rotation. The specimen was then
25 centered and rotated over 180° with a rotation step of 0.1°. A 40 keV X-ray beam passed through
26 the specimen, producing projection images with an average 6-8 scans at each rotation step. The
27 projection images had an identical size of 4904 × 3280 pixels. The resolution was selected to be
28 1.0-1.6 μm/pixel. The reconstruction was performed by using NRecon software (Micro Photonic
29 Inc., Allentown, PA, USA) to obtain the individual 2D slices, followed by 3D reconstruction in
30 the software CTVox.

1 SEM was used to provide higher-resolution observations of the composites' microstructures.
2 Traditional metallographic polishing was first conducted on the composite specimens. The
3 specimens were then sputter-coated with platinum at the polished surfaces. SEM images at high
4 resolution were obtained by using a FEI NovaNano SEM (Hillsboro, OR, USA). Furthermore,
5 SEM images were taken to determine the specimen's fiber volume fraction (FVF). For each
6 specimen, five different $125 \times 105 \mu\text{m}^2$ regions were randomly selected to count the fibers in pixel
7 size, and finally calculate the averaged FVF.

8

9 3.2. d-SENB experiments with integration of ultrafast X-ray imaging technique

10 To investigate the composites' low-velocity impact responses, a modified split-Hopkinson
11 pressure bar technique was utilized to perform the d-SENB experiments and apply dynamic three-
12 point flexural loadings to the notched composite specimens. The real-time damaging process was
13 visualized by integrating an ultrafast X-ray imaging with the split-Hopkinson pressure bar. Figure
14 3 schematically illustrates the integrated experimental setup.

15 Compared with the traditional split-Hopkinson pressure bar, the modified bar in this study
16 employed a 22241 N (5000 lbf) Kistler quartz load cell (Amherst, NY, USA) to substitute the
17 transmission bar. This enables to fit the entire loading setup into the compact X-ray hutch at
18 Argonne National Laboratory. Figure 4 is a photo showing the configuration near a specimen
19 before loading. The specimen was positioned between two supporting pins and an indenter pin,
20 and the notch tip was aligned with the indenter pin's center. The supporting pins were on an
21 adapted fixture installed with a 12.7-mm-diameter steel incident bar. A dynamic experiment
22 started from firing a gas gun, which accelerated a steel striker to impact the incident bar. The striker
23 had a length of 305 mm and a same diameter to the incident bar. An incident wave (ε_I) was
24 generated at the impacted end *A*. It traveled along the bar and was partially reflected back at the
25 opposite bar end *B*. Such a stress wave reflection stimulated the movement of the incident bar. The
26 specimen was subsequently prompted to move and was loaded by the indenter pin. A pair of strain
27 gauges were adhered on the incident bar's surfaces at the middle length, which recorded the
28 incident (ε_I) and reflected (ε_R) waves (see Fig. 3*a*). Such a wave propagation progression was
29 assumed to be one-dimensional, making the speed (v_B) and movement (S_B) of the incident bar
30 determined by equations (1) and (2) [20]

1
$$v_B(t) = c_B \cdot [\varepsilon_I(t) - \varepsilon_R(t)] \quad (1)$$

2
$$S_B(t) = \int_0^t v(\tau) d\tau \quad (2)$$

3 It is noted that the indenter pin was immovable, which was on an adapted fixture rigidly connected
4 with a load cell and then a backstop. Therefore, the specimen's deflection (S) at the loading point
5 and the loading speed (v) are equivalent to the movement and speed of the incident bar,
6 respectively. During a d-SENB experiment, the load cell directly measured the load history, as
7 shown in Fig. 3b. The specimen's deformation was constrained within a single pulse, which also
8 avoided repeated application of the dynamic loading and overload on the force transducer.

9 An *in-situ* visualization methodology was utilized to capture the damage process of the composite
10 specimen from the side by using the ultrafast X-ray imaging. As demonstrated in Fig. 3, during
11 the dynamic experiment, the high-intensity X-rays were perpendicular to the specimen's surface
12 and went through its thickness (B). The X-ray beam, with a spot size of 1-2 mm adjusted by two-
13 dimensional (2D) slits, was focused on the specimen at a small area between the specimen's notch
14 tip and the indenter pin. A group of slow and fast shutters were positioned between the 2D slits
15 and the specimen, decreasing the exposure duration of the specimen and the subsequent optics to
16 the X-rays and inhibit the radiation damage. During a d-SENB experiment, the reverse impact
17 technique drove the specimen to impact the static indenter pin, which allows the specimen's
18 damaging and failure phenomenon at the notch front to always appear within the X-ray window
19 for imaging. In this study, a propagation-based phase-contrast imaging was adopted to enhance the
20 contrast between different phases. After transmitting the specimen, the X-rays propagated in a free
21 space, which modulated the intensity and yielded the edge enhancement [21] to differentiate the
22 fiber, matrix, and the air due to damage development. A scintillator was placed downstream to
23 convert these X-ray sources to visible light information. A 45° mirror then reflected the converted
24 light source to a 5X objective lens for magnification. Finally, the magnified damage information
25 was recorded by a Shimadzu Hyper Vision HPV-X2 high-speed camera (Shimadzu, Kyoto, Japan).
26 The frame rate was designated to be ~0.5-1 M frames per second (fps) and the exposure time was
27 200 ns. A total of 256 frames were recorded in each experiment with the identical image size of
28 400 × 250 pixels and a resolution calibrated to be ~6.4 μm/pixel. The experiment on each specimen
29 type was repeated four to five times.

1 Integration of the ultrafast X-ray imaging technique into the dynamic loading setup requires to
2 synchronize the gas gun firing, double-window timing which is controlled by the fast and slow
3 shutters, dynamic event, and image recording. The trigger scheme was realized with the assistance
4 of several digital delay generators (DG535), which was demonstrated in Fig. 5. To start with, a
5 DG535 delivered a single-shot signal to turn on the solenoid valve and fire the gas gun. The striker
6 was launched. The slow shutter was activated to open at t_2 by a delayed signal, of which the time
7 span on average was determined via ten testing shots prior to the normal dynamic experiments. A
8 corresponding delayed signal was sent by DG535 to force the slow shutter to close at t_3 . Within t_2
9 and t_3 , the strain gauges captured the incident pulse and the rising signal triggered the oscilloscope
10 at t_0 . The fast shutters were manually turned on before each experiment. A delayed signal, of which
11 the time spacing was approximately determined by assuming an 1D wave propagation from the
12 strain gauge position to the bar end B , triggered the fast shutter DG. The fast shutter DG then
13 triggered the high-speed camera immediately and sent out a delayed signal to initiate the closure
14 of the fast shutters at t_1 . This effectively constrains the entire dynamic failure process within 256
15 frames to be recorded at a specified speed between t_0 and t_1 .

16

17 3.3. d-SENB experiments with integration of DIC

18 As shown in Fig. 4, when a notched composite specimen was dynamically loaded by the indenter
19 pin on the split-Hopkinson bar, the compressive stress wave, which was initiated at the supporting
20 pin/specimen contact area, needed time to transmit through the specimen and the adapted fixture.
21 Therefore, the load signal experienced a delay, of which the time duration can reach ~15% of the
22 entire loading time [11]. To determine the delay time of the load signal during a d-SENB
23 experiment on a steel specimen, Foster [22] modeled the stress wave's traveling process through
24 the incident bar and specimen. In this work, the stress wave propagation in the specimen was
25 experimentally monitored by virtue of DIC. The specimen was painted with random surface
26 texture and dynamically loaded on the modified split-Hopkinson pressure bar. The Shimadzu high-
27 speed camera, connected with a +2 close-up lens, observed from the side the patterns' movement.
28 A front light source was provided by a Cordin flash lamp system (Salt Lake City, UT, USA) for
29 illumination. The small patterns' displacement data provided the critical information to calculate
30 the specimen's surface deformation and thereby track the stress wave propagation. It is noted that
31 before the stress wave arrived at the load cell, it also needed to pass through the adapted steel

1 fixture to hold the indenter pin. Therefore, the total delay time (t_d) should include the wave
2 propagation in both the specimen (t_s) and the fixture (t_f) as

$$3 \quad t_d = t_s + t_f \quad (3)$$

4 where t_s was determined by tracking the stress wave propagation based on the strain field measured
5 through DIC, while t_f was calculated by assuming a 1D wave propagation through the steel fixture
6 length of 17 mm with an identical speed of 5189 m/s.

7

8 3.4. Quasi-static SENB experiments

9 A lab-constructed miniaturized material test system was used to measure the mechanical responses
10 of the notched composite specimens under quasi-static three-point bending loads. The
11 experimental setup is schematically illustrated in Fig. 7a. A close-up image of the loading
12 configuration is shown in Fig. 7b. Identical to the dynamic experimental setup, the specimen was
13 sandwiched between two supporting pins and an indenter pin. The fixture to hold the indenter pin
14 was connected to an actuator with the movement controlled by a displacement controller. On the
15 other side of the composite, the supporting pins' fixture was rigidly mounted to a 5000-lbf quartz
16 load cell and a fixed circular plate. During loading, the actuator drove the indenter pin to load on
17 the specimen. The indenter pin's movement was measured by a displacement sensor, and the load
18 history on the indenter pin was recorded by the load cell, which were equivalent to the composite
19 specimen's deflection and force at the loading point, respectively. Two loading speeds were
20 investigated, 0.06 mm/s, 1.20 mm/s.

21

22 3.5. Post-fracture analysis

23 After the mechanical experiments, representative fractured specimens were selected and
24 reconstructed by 3D X-ray computed tomography with the same parameters in Section 3.1. Due
25 to the limited field of view, only the area close to the notch tip was reconstructed to identify the
26 damage inside the composite in three dimensions. Several representative fractured specimens were
27 also picked and sputter-coated by platinum, and the fracture surfaces were imaged with higher
28 resolution by SEM.

29

30

31

1 **4. Results and Discussions**

2 4.1. Microstructures of the S-2 glass FRPMCs

3 Figure 8a presents the reconstructed 3D image and a 2D slice of a representative S-2 glass FRPMC
4 specimen. With a resolution of 1.0-1.6 $\mu\text{m}/\text{pixel}$ for each slide, the micro-CT scanner can identify
5 single S-2 glass fibers inside the composite. According to the variation of attenuation after the X-
6 ray penetrated through different materials, the fiber and matrix phases can be differentiated, and
7 fibers are colored brown in the reconstructed 3D image in Fig. 8a. The fiber distribution and
8 matrix-rich region are thereby recognized. Figure 8b provides a 2D SEM image of a polished
9 composite specimen's surface, which reveals, with a higher resolution, the S-2 glass fibers
10 embedded in the TGDDM-Jeffamine[®] D230+mPRS matrix. The fiber volume fraction was 69.74%
11 $\pm 8.35\%$ by averaging the fiber volume fraction measured by 2D SEM images. Since the 0° and
12 90° composite specimens were all sectioned from one composite laminate, their fiber and matrix
13 volumes were quantified with the same fiber volume fraction.

14

15 4.2. Load-deflection curve correction considering wave propagation in composites and fixture

16 As demonstrated in Section 3.3, for a d-SENB experiment, the load measurement must consider
17 the time delay resulting from the stress wave transmitting the specimen (t_s) and the adapted fixture
18 (t_f) before arriving at the load cell. In this study, t_s was measured by tracking the strain field
19 variation along the z -axis (indicated in Fig. 2) in the composite specimen. The computation was
20 performed on the obtained high-speed image sequences by using Vic-2D. To begin with, a region
21 of interest (ROI), covering the black-on-white painted specimen, was selected from an image
22 sequence, with the notched area cropped. Then, many small sub windows, identically having a size
23 of 24×24 pixels, were designated and divided the ROI. Subsequently, the correlation was carried
24 out with a step size of 2 pixels. The surface strain field was computed by tracking the sub windows'
25 grayscale value change corresponding to the speckle patterns' movement. Indicated in Fig. 6b, a
26 point M , located at the contact area between the specimen and one supporting pin, was chosen as
27 the starting point when the stress wave transmitted the specimen. The strain ϵ_{zz} at point M against
28 the time/frame number is extracted and plot in Fig. 9. The frame number when the stress wave
29 passed point M was determined to be n_M since the compressive strain value started to grow.
30 Correspondingly, ϵ_{zz} at another point N at the indenter pin/specimen contact area was tracked to

1 identify the frame number (n_N) when the stress wave arrived at the indenter pin. Consequently, the
2 time for the stress wave to transmit the composite specimen's thickness was calculated

$$3 \quad t_s = (n_N - n_M) \cdot \Delta t \quad (4)$$

4 where Δt is the frame time, which is 2 μ s in this study. For every composite type (0° and 90°),
5 experiments were repeated for five times and the corresponding t_s was computed in average. It is
6 worth noting that the determination of t_s is highly influenced by the frame rate and the speckle
7 pattern size. The average total delay time needs to consider the stress wave propagation in the
8 adapted fixture and was calculated by Eq. (3). Finally, the force-deflection curve for each specimen
9 type was corrected by shifting the original curve with an averaged distance of $\Delta S = v \cdot t_d$, where v
10 is the average impact velocity of 6.6 m/s. t_s , t_f , t_d , and ΔS for each composite type are summarized
11 in Table 3. The original and corrected force-deflection curves of a representative specimen are
12 presented in Fig. 10. More details of the method can be found in our previous work [11].

13

14 4.3. Dynamic fracture processes of different unidirectional composites

15 The dynamic failure processes of different unidirectional S-2 glass/TGDDM-Jeffamine[®] D230 +
16 mPRS composites were visualized by ultrafast X-ray imaging. The crack initiation and propagation,
17 variation of material's morphology during cracking, and physical features leading to the final
18 fracture were identified and reported with ultrafast X-ray images in this section and videos in the
19 supplementary materials. The ultrafast X-ray images, as shown in Figs. 11 and 13, are correlated
20 to the corrected force-deflection curves in Figs. 12 and 14, respectively, to track the mechanical
21 response of the specimen with different damaging characteristics. Before each dynamic
22 experiment, the specimen was aligned with the notch tip appearing close to the left edge of the
23 imaging window. The indenter was positioned outside the view window at the right. The fibers are
24 oriented at 0° and aligned with the vertical direction of the window, while the 90° fibers are
25 perpendicular to the window plane.

26

27 4.3.1. Dynamic fracture process of the 0° unidirectional composite

28 Figure 11 demonstrates the dynamic failure process of a representative unidirectional 0° S-2
29 glass/TGDDM-Jeffamine[®] D230 + mPRS composite specimen, with the corresponding video
30 provided as the electric supplementary material. As shown in Fig. 11a, the specimen first
31 experienced transverse compression by the indenter and was bent at the loading point. The notch

1 was blunt, deforming the material at the notch tip. However, such a deformation did not induce
2 observable fiber breakage and the transverse cracking of the material, owing to the high stiffness
3 and strength of S-2 glass fibers in both longitudinal and transverse directions. The crack was
4 initiated in Fig. 11*b* and then quickly deflected and propagated along the fibers in Fig. 11*c*, causing
5 the intralaminar delamination. By correlating the initial crack in Fig. 11*b* and the propagating crack
6 in Fig. 11*c* with the specimen's force-deflection curve in Fig. 12, it is revealed that the crack
7 initiation and propagation did not decrease the specimen stiffness immediately. With loading, the
8 specimen had a sudden stiffness variation (a kink on the force-deflection curve in Fig. 12), which
9 is presumably owing to the unloading of the partial failure by the intralaminar delamination outside
10 the window [23]. At the indenter side, the high stress concentration under the indenter increased
11 the misalignment of fibers and induced the compressive deformation in Fig. 11*d*.

12

13 4.3.2. Dynamic fracture process of the unidirectional 90° composite

14 Figure 13 depicts the fracture process of a representative unidirectional 90° composite specimen
15 in a d-SENB experiment. The corresponding video can be found in the supplementary material.
16 Due to the change of the fiber direction, the X-ray intensity becomes different in Fig. 13, which
17 results in a different pattern of the 90° composite specimen compared with that in Fig. 11. Upon
18 loading, the specimen was impacted onto the indenter pin at the right and experienced a transverse
19 compression by the indenter pin, and the notch was blunt, as observed in the video. The crack
20 initiated in Fig. 13*b* and then propagated to the indenter side and partitioned the specimen, which
21 is presented in Fig. 13*c*. As the loading continued and the crack opened, the fibers behind the crack
22 front bridged the crack and hindered the crack opening, indicating the transverse debonding
23 between the fiber and matrix (see Fig. 13*d*). These fibers were stretched and the matrix bonding
24 the fibers were deformed. Finally, these fibers bridging the crack debonded with the matrix from
25 one end, which can be identified by the video. The corresponding load-deflection curve is recorded
26 in Fig. 14, revealing that the initiated crack decreased the specimen's stiffness under the dynamic
27 loading. Besides, the load capacity of the 90° composite specimen was less than 2.5% of the
28 loading capacity of the 0° composite, but the mechanical behavior was more ductile.

29 The crack in the 90° composite has been believed to initiate due to the matrix cracking at the notch
30 tip and propagate along the fiber/matrix interface [24-26]. Such mechanisms were demonstrated
31 based on the real-time visualization on the composite's surface damage much below a single fiber

1 scale by using either optical imaging [24] or SEM [25-26]. However, the current X-ray imaging
2 setup does not have a sufficient spatial resolution and contrast to capture the fracture behavior
3 below the single-fiber scale, making it impossible to observe the matrix cracking at the crack
4 initiation and the fiber/matrix debonding during crack propagation. In addition, the crack
5 deflection along the fiber/matrix interface and the fiber bridging mechanism were believed to
6 contribute to the fracture toughness and increase the energy dissipation of the composite material
7 [27].

8

9 4.4. Loading rate effect on the composites' fracture behaviors

10 To assess the influence of the loading rate on the S-2 glass/TGDDM+Jeffamine[®] D230+mPRS
11 composite's fracture behavior, quasi-static SENB (q-SENB) experiments were conducted on the
12 composites and compared with the d-SENB experiments. The composites' force and deflection
13 responses, energy dissipation, stiffness, and fracture toughness were quantified at different loading
14 speeds and compared. The reconstructed 3D images by micro-CT scanning and higher resolution
15 2D SEM images of the fractured specimens provide a physical comparison of the composites'
16 damage evolution at different loading rates.

17

18 4.4.1. Force and deflection responses, stiffness and energy dissipation of the 0° composite

19 Figure 15 compares the load-deflection curves of the 0° composite specimens at different loading
20 rates. Different from the dynamic behavior, the composite failed in a ductile manner when the
21 loading speeds were 0.06 mm/s and 1.20 mm/s. Furthermore, in a dynamic event, delamination
22 may partially fracture the material and suddenly unload the specimen, inducing a kink on the force-
23 deflection curve [23]. The specimen maintained its original stiffness until reaching a higher load
24 capacity. In contrast, composites under quasi-static loadings experienced delamination at multiple
25 times, which gradually unloaded the specimens. The stiffness was reduced after each delamination,
26 and the load capacity could not reach the first peak load. The bending stiffness of the composite
27 was determined by linearly fitting the force-deflection curve before the deflection was 150 μm
28 based on the small-deformation assumption in elasticity. The average bending stiffnesses of the 0°
29 composites at different loading rates are compared in Fig. 16. It is revealed that the bending
30 stiffness experienced few changes when the loading speed increased from 0.06 mm/s to 1.20 mm/s.
31 However, it was increased by ~13% when the composite was dynamically loaded at a 6.6 m/s

1 velocity. Such an increase may be due to the dynamic strengthening of matrix and fibers under
2 transverse loadings [6, 9]. The energy dissipation was also increased at the high loading velocity
3 of 6.6 m/s. As shown in Fig. 17, the energy dissipation was calculated by integrating the force-
4 displacement curve. The energy dissipation of the unidirectional 0° composites subjected to
5 dynamic loadings is more than 19% of that under quasi-static loadings.

6 7 4.4.2. Force and deflection responses, stiffness, energy dissipation, and fracture toughness of the 8 90° composite

9 The force and deflection curves of the unidirectional 90° composites at different loading rates are
10 compared in Fig. 18. Under the dynamic loading at a speed of 6.6 m/s, the maximum deflection
11 was increased by 65%, indicating a more ductile failure behavior. The bending stiffness of the 90°
12 composites at different loading rates was obtained by linearly fitting the force-deflection curve in
13 Fig. 18 before $S = 50 \mu\text{m}$. On the other hand, the energy dissipation was determined by integrating
14 the force-deflection curve until the specimen was completely unloaded to $F = 0$. Although the
15 bending stiffness did not show significant change at different loading rates (see Fig. 16), the
16 average energy dissipation at the loading speed of 6.6 m/s was 4.9 times that under quasi-static
17 loadings, which is demonstrated in Fig. 17. The increased energy dissipation was owing to the
18 increase of both strength and ductility when the composite was dynamically loaded, as revealed in
19 Fig. 18. Besides, the bending stiffness and energy dissipation of the unidirectional 90° composites
20 were less than 35% and 2% of that of the 0° composites, which indicates the fiber orientation effect
21 on the composites' fracture behavior. When the fibers were orientated in 90° , the fracture
22 mechanisms were mainly matrix cracking and fiber/matrix debonding, making the bending
23 stiffness and energy dissipation lower.

24 The fracture toughness of a matrix system is critical for the composite's damage resistance [28].
25 Under impact loading at a low speed, the composite has the damage normally initiating from matrix
26 cracking and then developing into the intralaminar delamination. Furthermore, for the cross-ply
27 composites, as the intra-ply crack grows and reaches the ply interface, the sudden change in
28 material characteristics can induce an increase of the shear stress. The intralaminar crack is
29 deflected, then stimulates the matrix cracking between two plies, and finally induces the
30 interlaminar delamination [29]. Therefore, matrix cracking generally can set off the intralaminar
31 and interlaminar delamination. With matrix cracking dominating the crack initiation, SENB

1 experiments on the 90° composites were typically conducted to quantify the Mode I fracture
 2 toughness. In this work, the composites' fracture toughness was described by using the critical
 3 stress intensity factor K_{Ic} . According to ASTM D5045-14, the stress intensity factor is represented
 4 as

$$5 \quad K_{Ic} = \left(\frac{F(t)}{BH^{1/2}} \right) f\left(\frac{a}{H} \right) \quad (5)$$

6 where $F(t)$ is the time-resolved load measurement in a dynamic experiment; $f(a/H)$ is a
 7 dimensionless function which can be represented by

$$8 \quad f\left(\frac{a}{H} \right) = 6\sqrt{\frac{a}{H}} \frac{1.99 - (a/H)(1 - a/H) [2.15 - 3.93 \cdot (a/H) + 2.7 \cdot (a/H)^2]}{[1 + 2 \cdot (a/H)](1 - a/H)^{3/2}} \quad (6)$$

9 The measurement K_{Ic} was validated based on the specimen size criteria. First, to satisfy the plane
 10 strain assumption, the specimen needs to be sufficiently wide. Furthermore, the specimen is
 11 supposed to have an acceptable unnotched depth ($H-a$) so that the plastic deformation is not
 12 excessively developed. The quantitative description of the specimen size criteria is

$$13 \quad B, a, (H - a) > 2.5 \left(\frac{K_{Ic}}{\sigma_y} \right)^2 \quad (7)$$

14 where σ_y represents the yield strength of the composite at the corresponding loading rate.

15 In this study, the composite's yield strength $(\sigma_y)_c$ was approximated on the basis of the "rule of
 16 mixtures"

$$17 \quad (\sigma_y)_c = (\sigma_y)_F V_F + (\sigma_y)_M V_M \quad (8)$$

18 where $(\sigma_y)_F$ and $(\sigma_y)_M$ are the loading-rate-related strength of S-2 glass fiber [28] and the
 19 compressive yield stress of matrix [5], respectively; V_F and V_M are the fiber and matrix volume
 20 fractions of the unidirectional composites shown in Table 2.

21 During a d-SENB experiment, the X-rays passed through a composite specimen, which allowed
 22 tracking the damage initiation in a spatial scale of 20 μm [10] and timing scale of 1 μs . The
 23 variation of the stress intensity factor during the crack initiation and propagation is quantified in
 24 Fig. 19. It is noted that ASTM D5045-14 standardizes the computation of the stress intensity factor
 25 under quasi-static loadings. The low loading speed usually enables the material to be fully
 26 deformed before crack initiation. Therefore, the peak force is used to calculate the stress intensity
 27 factor. However, under dynamic loading, the small crack may not be given sufficient time to extend,

1 so the composite can still have some stiffness to resist the external loading. The peak load may not
2 be reached at the crack initiation, which has been revealed in Fig. 14. Consequently, for the
3 dynamic stress intensity factor, the force at the crack initiation, measured by correlating the X-ray
4 images with the corrected force-deflection curves, was employed for calculation. Figure 19
5 compares the stress intensity factor of the 90° at various loading rates. Similar to the trend of the
6 energy dissipation, the stress intensity factor had a variation less than 5% when the loading speed
7 changed from 0.06 mm/s to 1.20 mm/s. However, it was increased by ~110% under dynamic
8 loadings.

9 10 4.4.3. Post-fracture images of composites at different loading rates

11 Figure 20 compares the unidirectional 0° composites' morphologies after the SENB experiments
12 at different loading speeds, which are obtained by the 3D X-ray computed tomography. After the
13 three-point bending loads were applied to the 0° composites at speeds of 0.06 mm/s and 1.20 mm/s,
14 the composites both show catastrophic failure by transverse compression under the indenter pin.
15 Kink band, fiber buckling, splitting, and delamination can be identified in the reconstructed
16 structures of the composites in Figs. 20*a* and 20*b*. On the other hand, the composite after the
17 dynamic loading in Fig. 20*c* had less damage develop, which is presumably because the specimen
18 was not fractured completely by the impact loading. Close to the indenter pin/specimen contact
19 area, a crack caused by the material's compressive failure was observed. The crack can be
20 correlated to the fiber micro buckling shown in Fig. 11*d*. It is noted that the crack did not penetrate
21 through the specimen's thickness, revealing that the ultrafast X-ray imaging technique can identify
22 damage inside the composite [10]. The damage zone was less than 20% of the composites under
23 quasi-static loadings.

24 The fracture surfaces of the unidirectional 90° composite specimens after loaded at different rates
25 are compared in Fig. 21. The specimens at two quasi-static loading rates had similar damage
26 extents, as shown in Figs. 21*a* and 21*b*. In contrast, the dynamically loaded composite specimen
27 shows a more-than-200% increase in the extent of damage observed as the fiber/matrix transverse
28 debonding in Fig. 21*c*. Furthermore, the damage is distributed more evenly on the fracture surface.

1 **5. Conclusions**

2 This study investigated the dynamic fracture of the S-2 glass fiber-reinforced ductile polymer
3 matrix composites. The matrix ductility was improved by a network topology modification
4 technique via mPRS [5]. The composite specimens were prepared and characterized by micro-CT
5 scanning and SEM prior to the mechanical experiments. A modified split-Hopkinson pressure bar
6 technique was employed to dynamically load the notched composite specimens with three-point
7 flexural loadings. By integrating the split-Hopkinson pressure bar loading methodology with the
8 ultrafast X-ray imaging technique, the dynamic fracture processes of the unidirectional 0° and 90°
9 composites were visualized in real time and correlated to the specimens' force and deflection
10 responses. Due to the stress wave propagation in the specimen and adapted fixture, a load signal
11 delay needs to be considered. The delay time was measured by performing extra dynamic
12 experiments and monitoring the specimen's surface deformation by using DIC. The specimens'
13 dynamic force-deflection curves were then corrected. Additional q-SENB experiments were
14 performed to assess the influence of loading rate on the composites' fracture behavior. The force
15 and deflection history, bending stiffness, energy dissipation, and fracture toughness were
16 quantified and compared. Post-fracture analysis by using the 3D X-ray computed tomography and
17 SEM provided physical observation on the composite's fracture morphology influenced by the
18 loading rate. The findings are concluded below:

19 (1) With high spatial and timing resolution, the *in-situ* radiography, ultrafast X-ray imaging,
20 provided an effective observation on the crack initiation inside the composite under dynamic
21 loading. This contributes to the accurate quantification of the composite's mechanical properties,
22 such as fracture toughness. Furthermore, the X-rays could penetrate through the opaque composite
23 and assist in capturing the internal microscale damage evolution during a dynamic loading event.

24 (2) When the loading speed was increased from 0.06 mm/s and 1.20 mm/s to 6.6 m/s, the variation
25 of the bending stiffness of the unidirectional 0° and 90° composites was less than 14%. However,
26 the energy dissipation could be improved by ~ 4.3 times when the composites were dynamically
27 loaded at a velocity of 6.6 m/s. Dynamic strengthening was observed in both composite types.

28 (3) The ductility and fracture toughness of the unidirectional 90° composite experienced an
29 increase of ~65% and ~110%, respectively, when the loading speed increased to 6.6 m/s.

30 (4) The unidirectional 0° composites after dynamic loadings had a damage zone less than 20% of
31 those under quasi-static loadings. This is possible because the composites did not completely fail

1 when the loads were dynamically applied on a split-Hopkinson pressure bar. On the other hand,
2 the 90° composites were fractured by the dynamic loads. The fracture surface demonstrated more
3 evenly distributed damage by the fiber/matrix transverse debonding, and the extent of damage was
4 increased by more than 2 times.

6 **CRedit authorship contribution statement**

7 Jinling Gao: Resources, Investigation, Formal analysis, Writing - original draft. Nesredin Kadir:
8 Investigation. Julio A. Hernandez: Resources. Jian Gao: Resources. Todd Horn: Resources.
9 Garam Kim: Resources. Kamel Fezzaa: Investigation. Tyler N. Tallman: Resources, Writing -
10 review & editing. Giuseppe R. Palmese: Resources. Ronald Sterkenburg: Resources. Weinong
11 Chen: Supervision, Writing - review & editing.

13 **Declaration of competing interest**

14 The authors declare that they have no known competing financial interests or personal
15 relationships that could have appeared to influence the work reported in this paper.

17 **Acknowledgments**

18 Research was sponsored by the Army Research Laboratory and was accomplished under
19 Cooperative Agreement Number W911NF-12-2- 0022. The views and conclusions contained in
20 this document are those of the authors and should not be interpreted as representing the official
21 policies, either expressed or implied, of the Army Research Laboratory or the U.S. Government.
22 The U.S. Government is authorized to repro- duce and distribute reprints for Government
23 purposes notwithstanding any copyright notation herein. This research used resources of the
24 Advanced Photon Source, a U.S. Department of Energy (DOE) Office of Science User Facility
25 operated for the DOE Office of Science by Argonne National Laboratory under Contract No.
26 DE-AC02-06CH11357. Funding for high-speed imaging equipment used in this work was
27 provided by AFOSR Award No. FA9550-16-1-0315 (Dr. Martin Schmidt, Program Officer).

29 **Appendix A. Supplementary data**

30 Supplementary data to this article can be found online at [https://doi.](https://doi.org/10.1016/j.compositesb.2022.109754)
31 [org/10.1016/j.compositesb.2022.109754](https://doi.org/10.1016/j.compositesb.2022.109754).

1 **References**

- 2 [1] Stickel JM, Nagarajan M. Glass fiber-reinforced composites: from formulation to application.
3 *Int J Appl Glass Sci* 2012; 3(2): 122-136.
- 4 [2] Karataş MA, Gökkaya H. A review on machinability of carbon fiber reinforced polymer (CFRP)
5 and glass fiber reinforced polymer (GFRP) composite materials. *Def Technol* 2018; 14(4): 318-
6 326.
- 7 [3] Jefferson AJ, Srinivasan SM, Arockiarajan A. Effect of multiphase fiber system and stacking
8 sequence on low-velocity impact and residual tensile behavior of glass/epoxy composite laminates.
9 *Polym Compos* 2019; 40(4): 1450-1462.
- 10 [4] Jefferson AJ, Vellayaraj A, Hom D. *Repair of Polymer Composites: Methodology, Techniques,*
11 *and Challenges.* Woodhead Publishing, 2018.
- 12 [5] Gao J, Chu X, Henry CK, Santos SC, Palmese GR. Highly ductile glassy epoxy systems
13 obtained by network topology modification using partially reacted substructures. *Polymer* 2021;
14 212: 123260.
- 15 [6] Sharifi M, Palmese GR. Ductile high-Tg epoxy systems via incorporation of partially reacted
16 substructures. *J Mater Chem A* 2021; 9(2): 1014-1024.
- 17 [7] Jordan JL, Foley JR, Siviour CR. Mechanical properties of Epon 826/DEA epoxy. *Mech Time-*
18 *Depend Mat* 2008; 12(3): 249-272.
- 19 [8] Siviour CR, Jordan JL. High strain rate mechanics of polymers: a review. *J Dynamic Behavior*
20 *Mater* 2016; 2(1): 15-32.
- 21 [9] Gao J, Lim BH, Zhai X, Nie Y, Kedir N, Chen W. Failure behaviors of single high-performance
22 fibers under transverse dynamic cut. *Int J Impact Eng* 2020; 144: 103660.
- 23 [10] Gao J, Kedir N, Kirk CD, Hernandez J, Wang J, Paulson S, Zhai X, Horn T, Kim G, Gao J,
24 Fezzaa K, De Carlo F, Shevchenko P, Tallman TN, Sterkenburg R, Palmese GR, Chen W. Real-
25 time damage characterization for GFRCs using high-speed synchrotron X-ray phase contrast
26 imaging. *Compos Part B Eng* 2021; 207: 108565.
- 27 [11] Gao J, Kedir N, Kirk CD, Hernandez JA, Wang J, Paulson S, Zhai X, Horn T, Kim G, Fezzaa
28 K, De Carlo F, Shevchenko PD, Tallman TN, Sterkenburg R, Chen W. High-speed synchrotron
29 X-ray phase-contrast imaging for evaluating microscale damage mechanisms and tracking
30 cracking behaviors inside cross-ply GFRCs. *Compos Sci Technol* 2021; 210: 108814.

- 1 [12] Zhuang L. Failure mechanisms in unidirectional composites under transverse and longitudinal
2 tension, Ph.D. Dissertation, Texas A & M University, College Station, 2018.
- 3 [13] Sanders RC, Edge EC, Grant P. Basic failure mechanisms of laminated composites and related
4 aircraft design implications. *Composite Structures 2*, Springer, Dordrecht, 1983.
- 5 [14] Ekşı S, Genel K. Comparison of mechanical properties of unidirectional and woven carbon,
6 glass and aramid fiber reinforced epoxy composites. *Composites 2017*; 132: 879-882.
- 7 [15] Gao J, Kirk CD, Kedir N, Paulson S, Hernandez J, Gao J, Zhai X, Wang J, Horn T, Kim G,
8 De Carlo F, Shevchenko P, Tallman TN, Palmese G, Sterkenburg R, Chen, W. A method for
9 characterization of multiple dynamic constitutive parameters of FRCs. *Compos Sci Technol 2021*;
10 203: 108607.
- 11 [16] Tan KT, Watanabe N, Iwahori Y, Ishikawa T. Effect of stitch density and stitch thread
12 thickness on compression after impact strength and response of stitched composites. *Compos Sci*
13 *Technol 2012*; 72(5): 587-598.
- 14 [17] Alpyildiz T, Icten BM, Karakuzu R, Kurbak A. The effect of tuck stitches on the mechanical
15 performance of knitted fabric reinforced composites. *Compos Struct 2009*; 89(3), 391-398.
- 16 [18] Gao J, Guo Z, Hernandez JA, Zhou F, Nie Y, Gao J, Lim BH, Kedir N, Zhai X, Wang J, Tsai
17 JT, De Carlo F, Shevchenko PD, Tallman TN, Jun MBG, Palmese GR, Chen W. Transverse impact
18 by RCCs on S-glass and Kevlar® FRC strips. *Compos Part A Appl Sci Manuf 2021*; 146: 106425.
- 19 [19] ASTM D 5045-14. Standard test methods for plane-strain fracture toughness and strain energy
20 release rate of plastic materials. ASTM International, West Conshohocken, PA: ASTM
21 International; 2007.
- 22 [20] Nie Y, Claus B, Gao J, Zhai X, Kedir N, Chu J, Sun T, Fezzaa K, Chen, WW. In situ
23 observation of adiabatic shear band formation in aluminum alloys. *Exp Mech 2020*; 60(2): 153-
24 163.
- 25 [21] Hudspeth M, Claus B, Dubelman S, Black J, Mondal A, Parab N, Funnell C, Hai F, Qi ML,
26 Fezzaa K, Luo SN, Chen W. High speed synchrotron X-ray phase contrast imaging of dynamic
27 material response to split Hopkinson bar loading. *Rev Sci Instrum 2013*; 84: 025102.
- 28 [22] Foster JT, Silling SA, Chen, W. An energy based failure criterion for use with peridynamic
29 states. *Int J Multiscale Comput Eng 2011*; 9(6): 675-688.

- 1 [23] Zhang X, Gao J, O'Brien D, Chen W, Ghosh S. Parametrically homogenized continuum
2 damage mechanics (PHCDM) models for analyzing composite structures. *Compos Part B Eng*
3 2021, accepted.
- 4 [24] Wafai H, Yudhanto A, Lubineau G, Mulle M, Alghamdi T, Thoroddsen ST, Yaldiz R,
5 Verghese N. In situ micro-scale high-speed imaging for evaluation of fracture propagation and
6 fracture toughness of thermoplastic laminates subjected to impact. *Compos Struct* 2019; 210: 747-
7 754.
- 8 [25] Montenegro DM, Bernasconi F, Zogg M, Gössi M, Libanori R, Wegener K, Studart AR.
9 Mode I transverse intralaminar fracture in glass fiber-reinforced polymers with ductile matrices.
10 *Compos Struct* 2017; 165, 65-73.
- 11 [26] Wafai H, Yudhanto A, Lubineau G, Yaldiz, R, Verghese N. An experimental approach that
12 assesses in-situ micro-scale damage mechanisms and fracture toughness in thermoplastic
13 laminates under out-of-plane loading. *Compos Struct* 2019; 207: 546-559.
- 14 [27] Vieille B, Gonzalez JD, Bouvet C. Fracture mechanics of hybrid composites with ductile
15 matrix and brittle fibers: Influence of temperature and constraint effect. *J Compos Mater* 2019;
16 53(10): 1361-1376.
- 17 [28] Andrew JJ, Srinivasan SM, Arockiarajan A, Dhakal HN. Parameters influencing the impact
18 response of fiber-reinforced polymer matrix composite materials: A critical review. *Compos Struct*
19 2019; 224: 111007.
- 20 [29] Tita V, de Carvalho J, Vandepitte D. Failure analysis of low velocity impact on thin composite
21 laminates: Experimental and numerical approaches. *Compos Struct*. 2008; 83(4): 413-28.

22

23 **Figure captions**

24 **Figure 1.** True stress-strain curves of the TGDDM-Jeffamine[®] D230 + mPRS matrix at different loading
25 rates (courtesy of Gao et al. [5]).

26 **Figure 2.** SENB experimental scheme.

27 **Figure 3.** Schematic of d-SENB experimental setup with integration of ultrafast X-ray imaging technique.
28 (a) Strain gauge signal; (b) Load measurement; (c) Ultrafast X-ray image sequence.

29 **Figure 4.** A photo of the d-SENB experimental scheme.

30 **Figure 5.** Timing sequence used throughout the d-SENB experiments with integration of ultrafast X-ray
31 imaging technique.

1 **Figure 6.** d-SENB experimental setup with integration of DIC. (a) Schematic diagram; (b) Specimen and
2 loading configuration. The scale bar has a width of 2 mm. The flashlight source was indeed perpendicular
3 rather than parallel to the specimen's surface.

4 **Figure 7.** Experimental setup of the q-SENB experiments. (a) Schematic diagram; (b) Specimen and
5 loading configuration.

6 **Figure 8.** Microstructures of the composites. (a) 3D reconstructed structure; (b) SEM image.

7 **Figure 9.** Surface strain histories at specimen's contacting points with the supporting pin (M) and the
8 indenter pin (N).

9 **Figure 10.** Correction of the force-deflection curve.

10 **Figure 11.** Time-resolved dynamic damage behavior of a unidirectional 0° S-2 glass/TGDDM-Jeffamine[®]
11 D230 + mPRS composite specimen. (a) $t = 0$, (b) $t = 34.04$, (c) $t = 73.60$, (d) $t = 119.60 \mu\text{s}$.

12 **Figure 12.** Force against deflection response of the 0° composite specimen in Fig. 11.

13 **Figure 13.** Time-resolved dynamic damage behavior of a unidirectional 90° composite specimen. (a) $t = 0$,
14 (b) $t = 22.08$, (c) $t = 44.16$, (d) $t = 66.24 \mu\text{s}$.

15 **Figure 14.** Force against deflection response of the 90° composite specimen in Fig. 13.

16 **Figure 15.** Comparison of the force-deflection curves of the representative 0° composite specimens at
17 various loading velocities.

18 **Figure 16.** Comparison of the composites' stiffness at different loading velocities.

19 **Figure 17.** Comparison of the composites' energy dissipation at various loading velocities.

20 **Figure 18.** Comparison of the force-deflection curves of the representative 90° composites under different
21 loading velocities.

22 **Figure 19.** Comparison of the stress intensity factor of the 90° composites at various loading velocities.

23 **Figure 20.** Reconstructed 3D images of the fractured representative 0° composites at different loading
24 velocities. $v =$ (a) 0.06 m/s; (b) 1.20 mm/s; (c) 6.60 m/s.

25 **Figure 21.** SEM images of the fractured representative 90° composites at various loading velocities. $v =$ (a)
26 0.06 m/s; (b) 1.20 mm/s; (c) 6.60 m/s (Arrows indicate damage due to fiber/matrix transverse debonding).
27
28
29

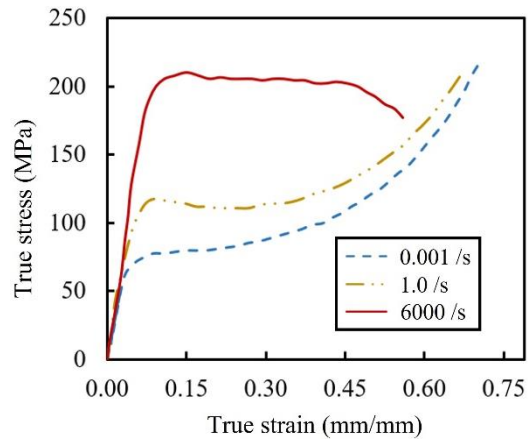


Figure 1

1
2
3
4
5
6

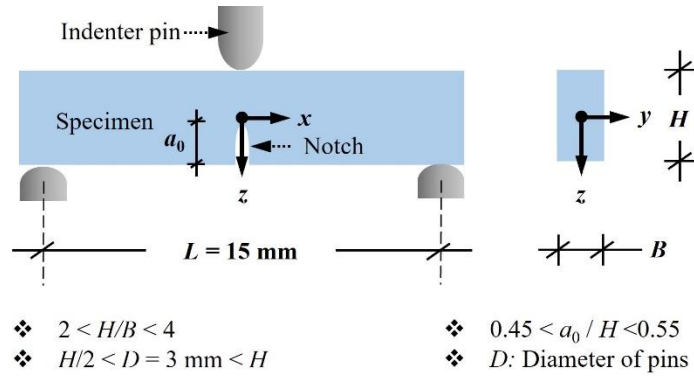


Figure 2

7
8
9

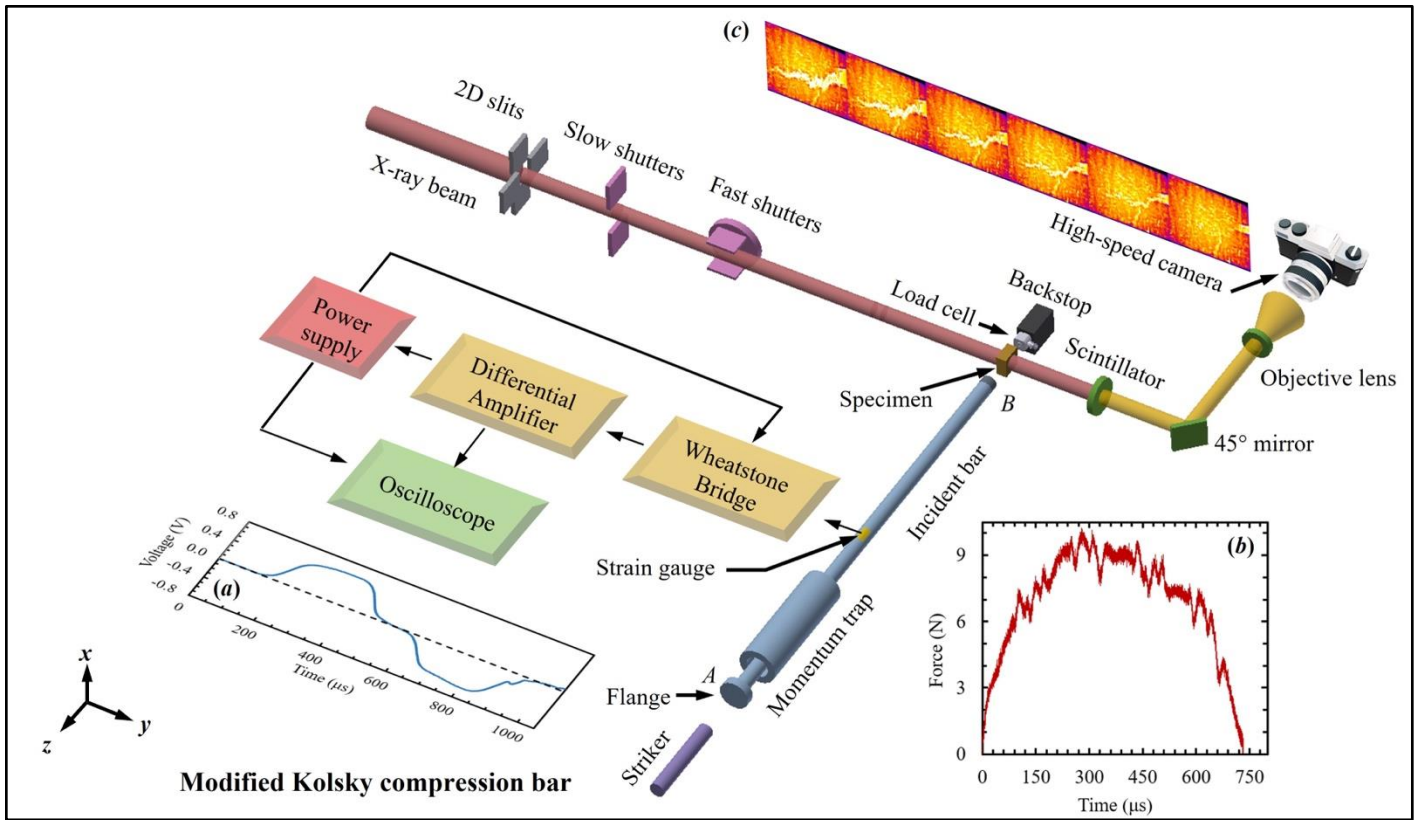


Figure 3

- 1
- 2
- 3
- 4

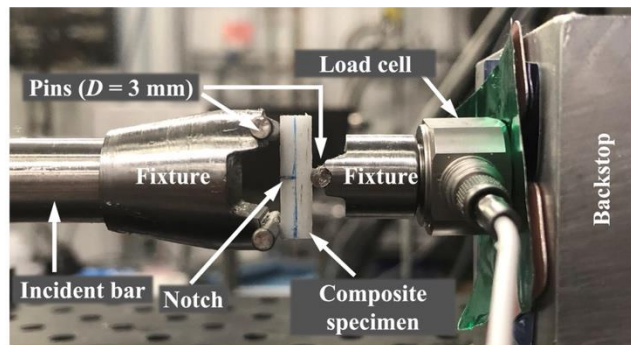


Figure 4

- 5
- 6
- 7
- 8
- 9
- 10

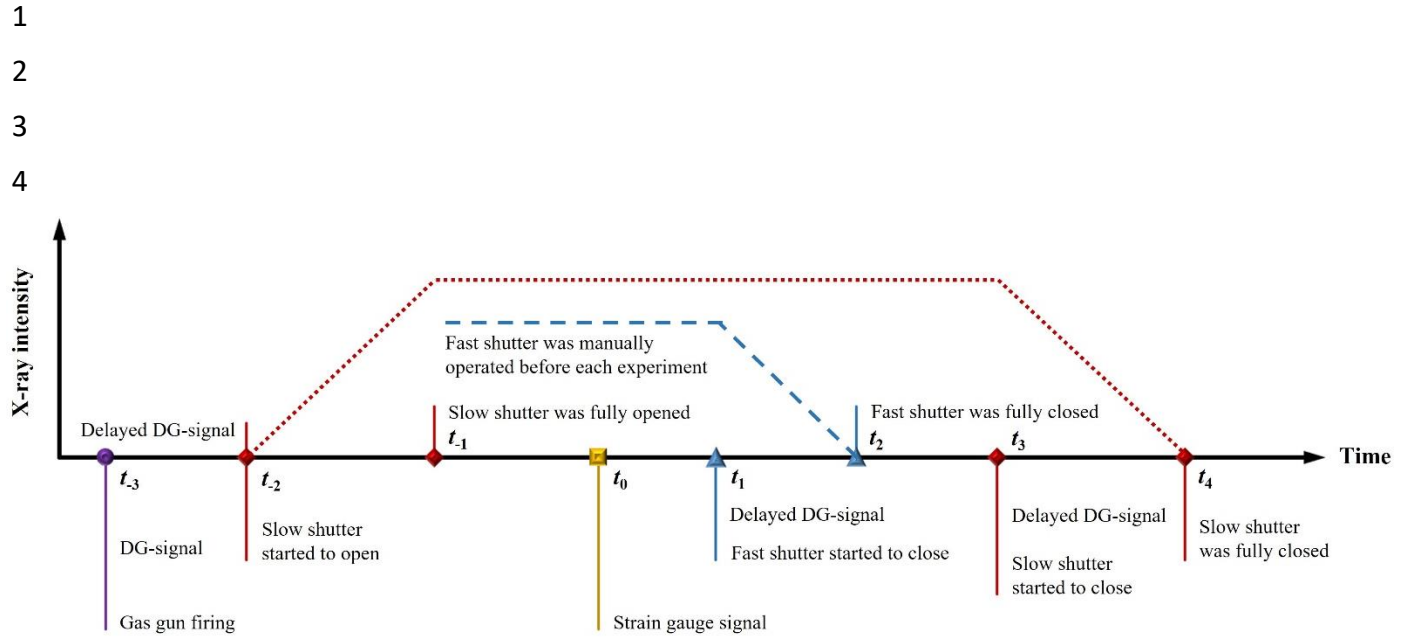


Figure 5

5
6
7
8

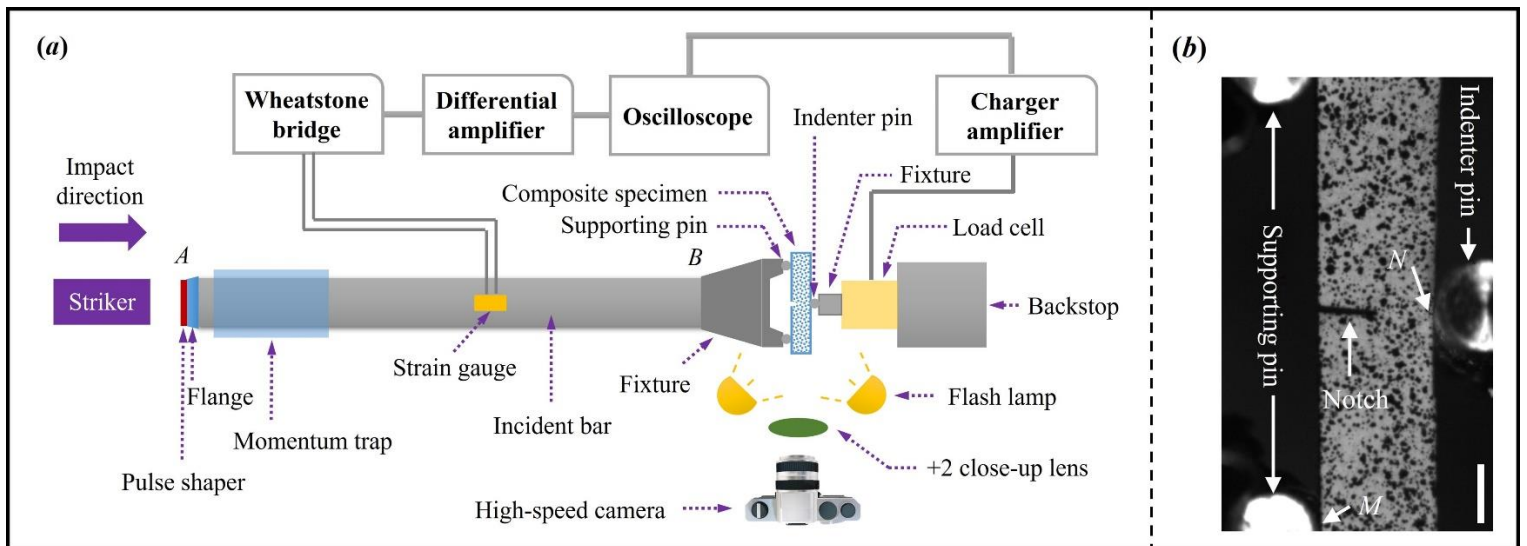


Figure 6

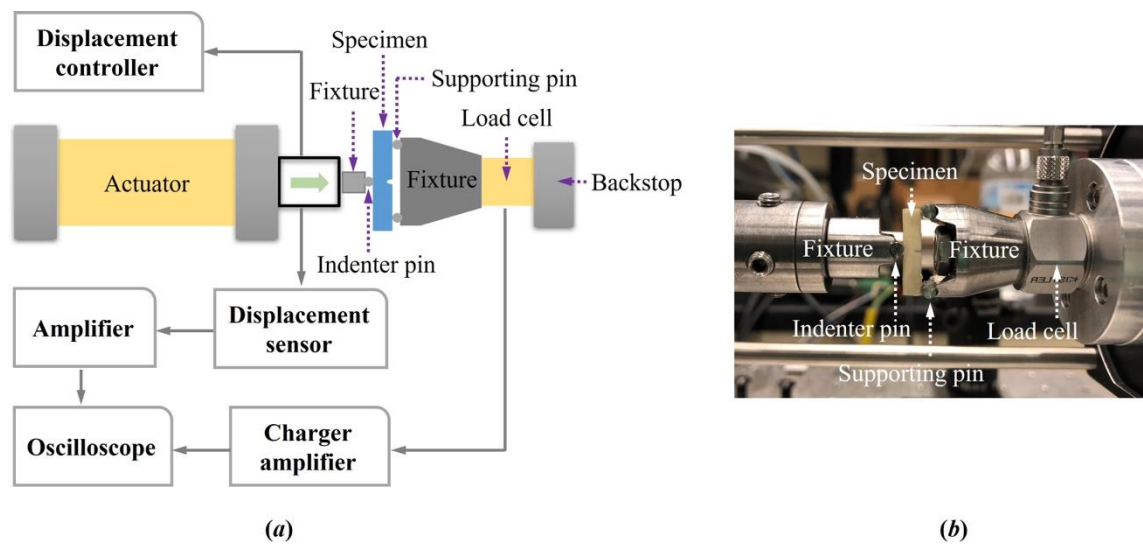


Figure 7

1
2
3
4
5
6

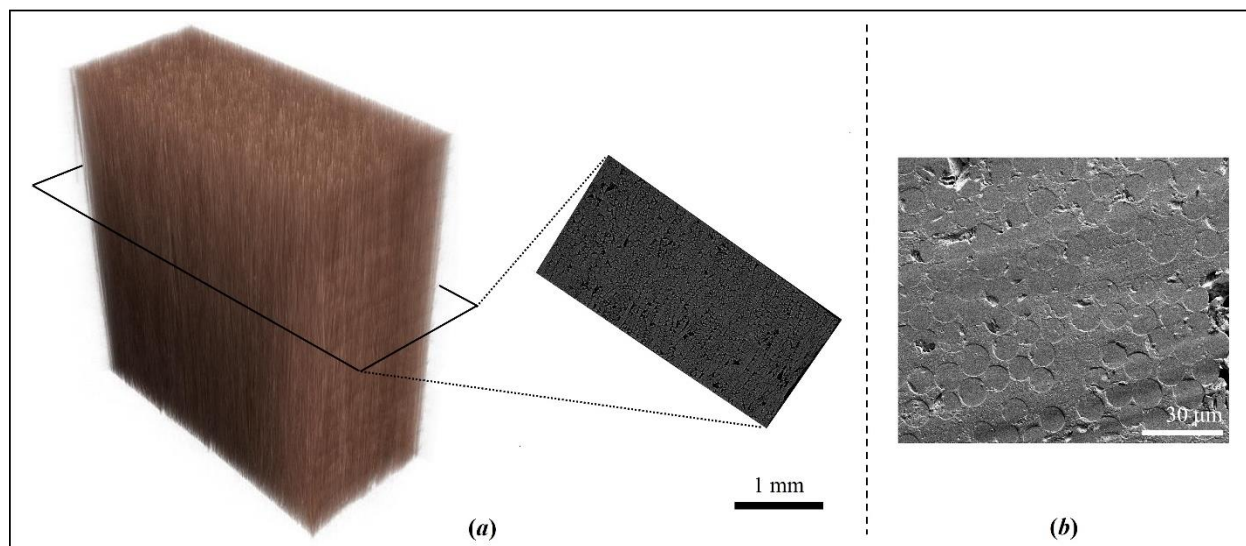


Figure 8

7
8
9
10

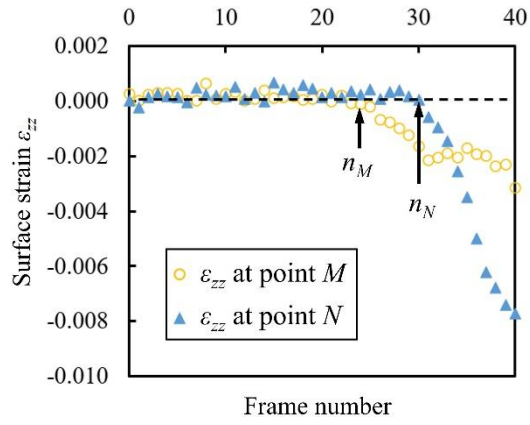


Figure 9

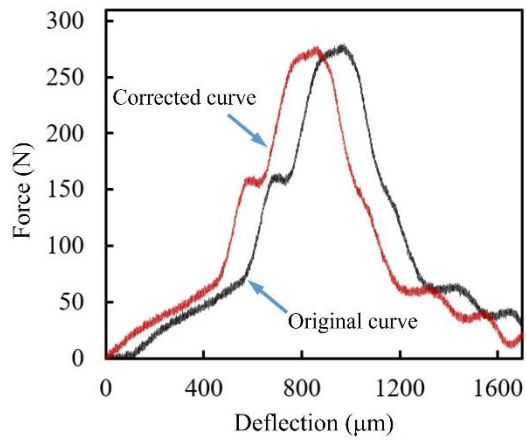


Figure 10

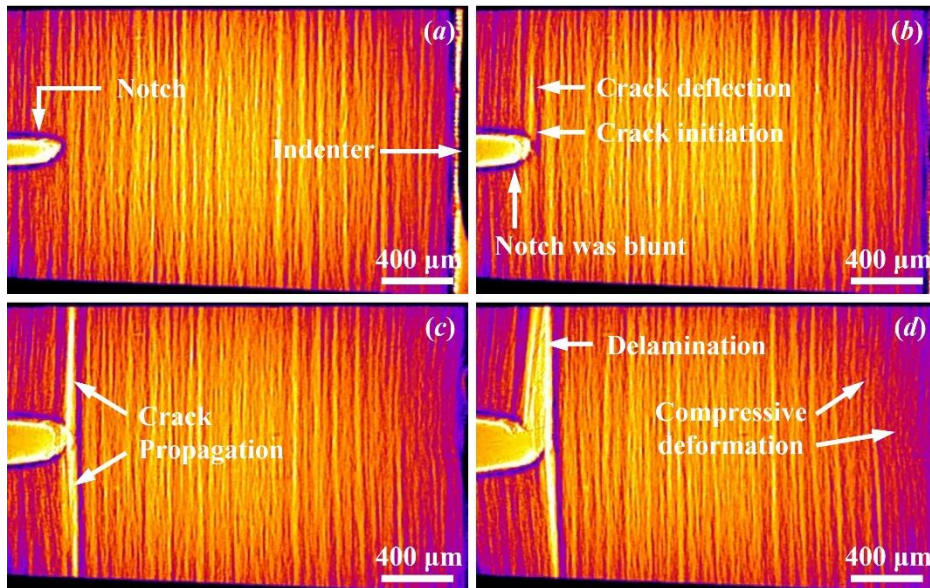


Figure 11

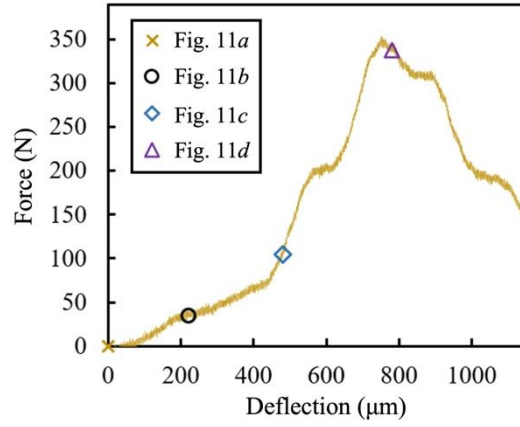


Figure 12

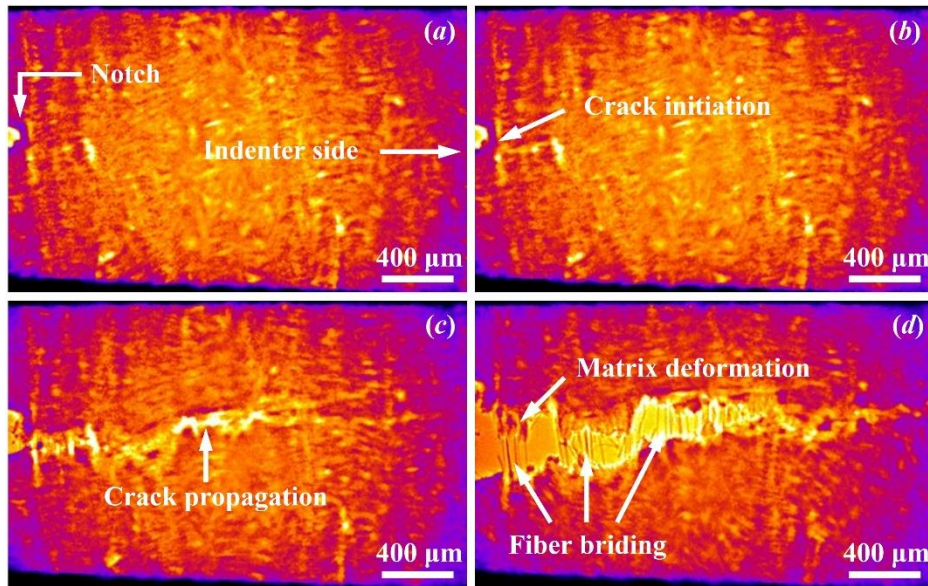


Figure 13

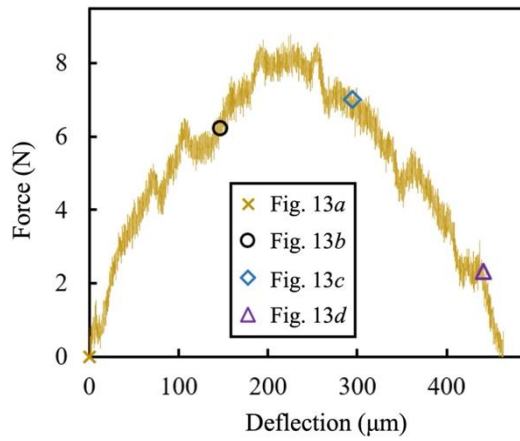


Figure 14

1
2
3

4
5
6

7
8

1

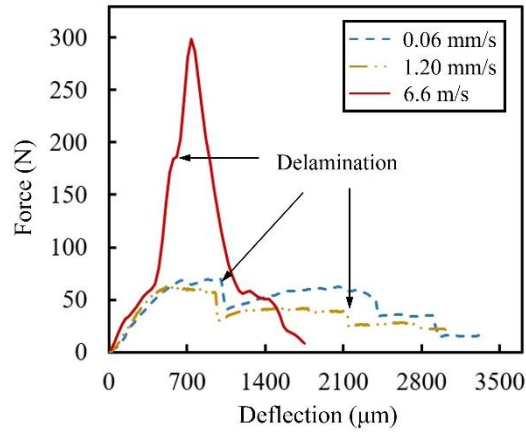


Figure 15

2

3

4

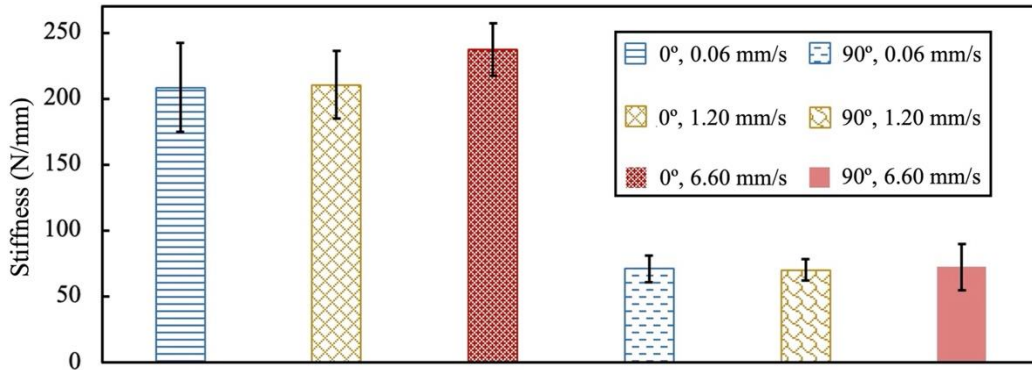


Figure 16

5

6

7

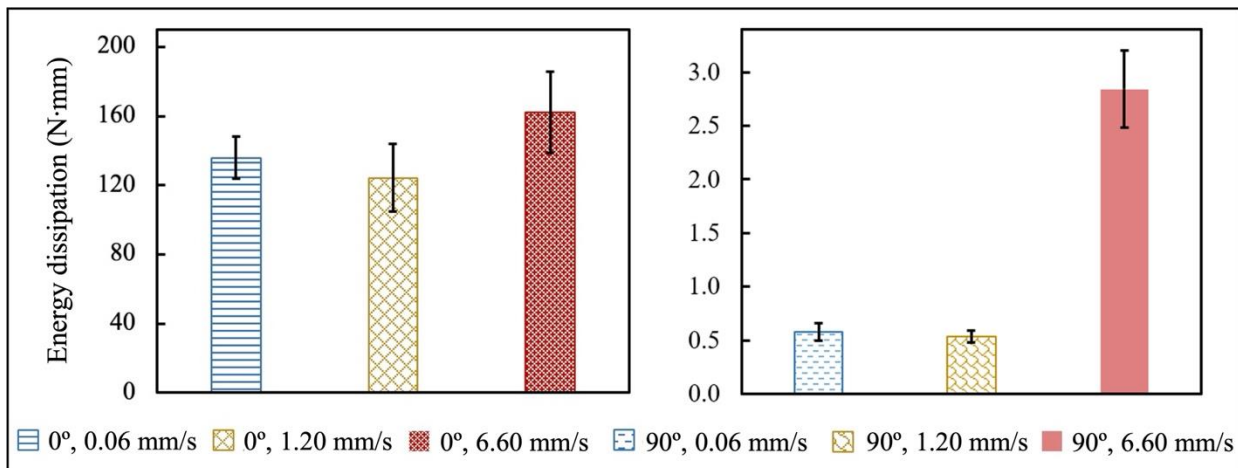


Figure 17

8

9

10

1
2
3

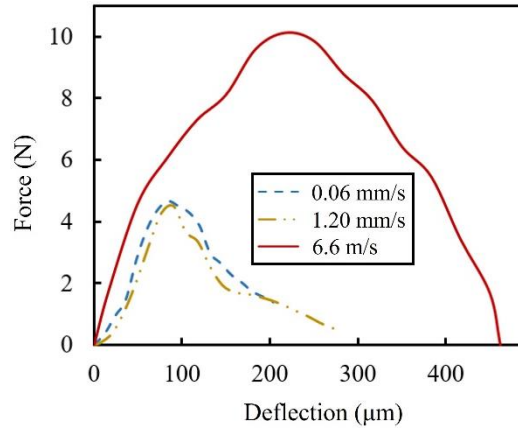


Figure 18

4
5
6
7
8

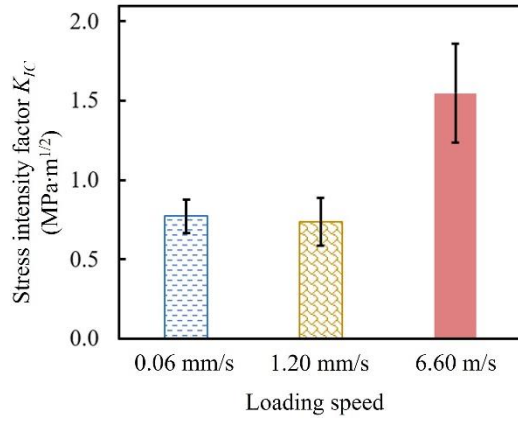


Figure 19

9
10
11
12
13

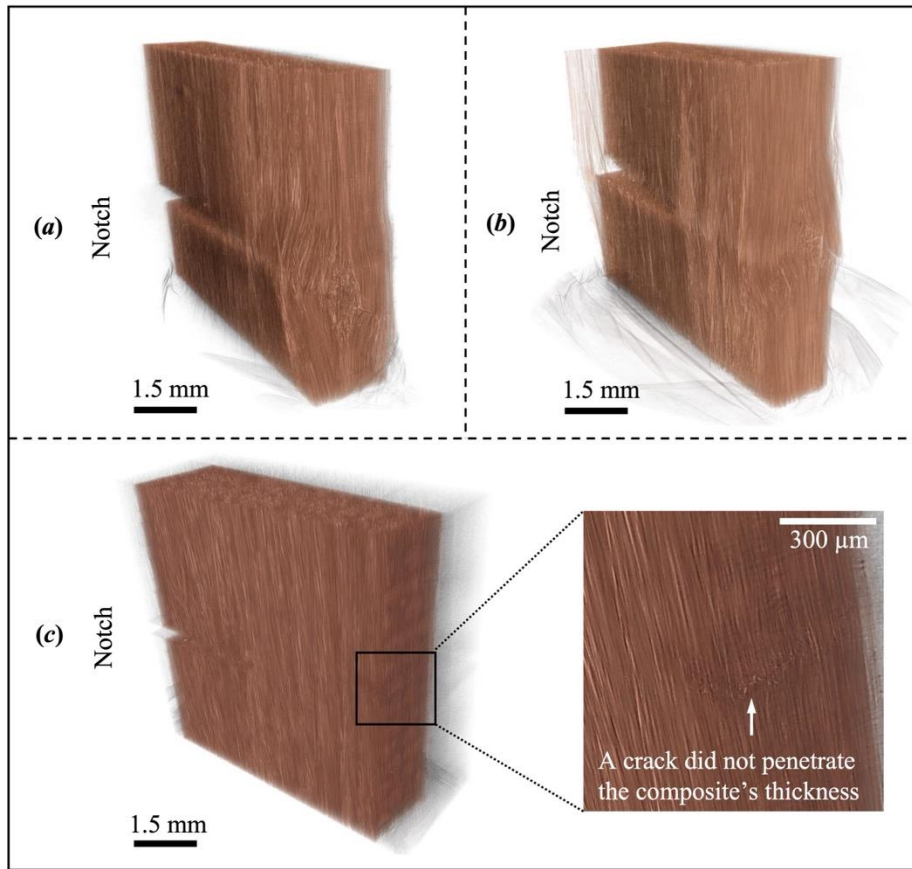


Figure 20

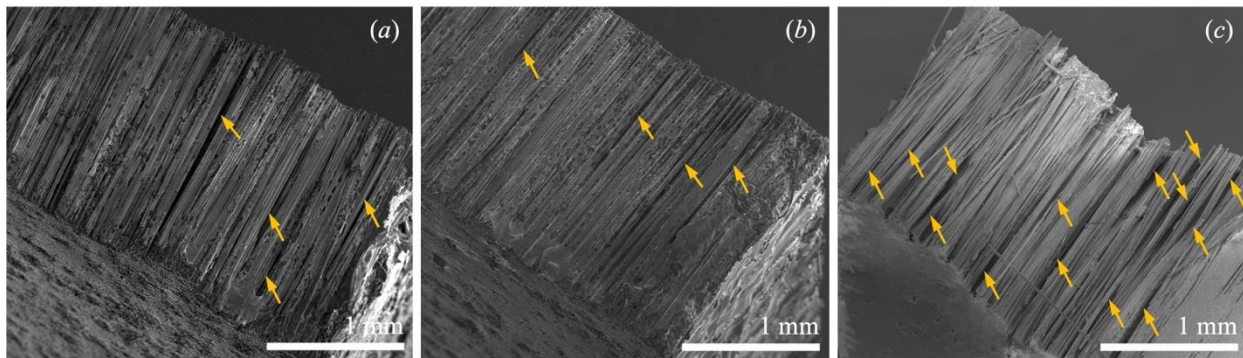


Figure 21

1
2
3
4
5
6
7
8
9
10
11

1

Table 1. Mechanical properties of TGDDM-Jeffamine® D230 + mPRS matrix [5]

Matrix	Failure strain (%)	Modulus (GPa)	Failure Strength (MPa)	Tg (°C)	K_{IC} (MPa·m ^{1/2})	G_{IC} (J·m ²)
Tension	21.3 ± 1.6	2.25 ± 0.06	57.6 ± 1.5	135	1.03 ± 0.03	415 ± 28
Compression	69.6 ± 2.3	2.29 ± 0.08	207.8 ± 6.8			

2

3

4

5

Table 2. Dimensions and fiber volume fractions of different unidirectional composites

Fiber orientation	L (mm)	H (mm)	B (mm)	a (mm)	Fiber volume fraction (%)
0°	15	3.77 ± 0.07	1.53 ± 0.17	1.93 ± 0.13	69.74 ± 8.35
90°	15	3.76 ± 0.08	1.57 ± 0.19	1.81 ± 0.08	

6

7

8

9

Table 3. Load signal delay and shifting distance of load-deflection curves for different composites.

Fiber orientation	0°	90°
t_s (μs)	13.1 ± 1.8	13.0 ± 2.1
t_f (μs)	3.3	3.3
t_d (μs)	16.4 ± 1.8	16.3 ± 2.1
ΔS (μm)	108.2 ± 11.9	107.6 ± 13.9

10